Observations of cosmic-ray Sun's shadow with LHAASO-WCDA

Ming-Yang Cui,[a,*] **Jie Xia,**[a,b] **Jia-Yin He,**[a,b] **Guang-Lu Shi,**[a,b] **Li Feng,**[a,b] **Qiang Yuan**[a,b] **and Yi Zhang**[a,b] **for the LHAASO collaboration**

[a]*Key Laboratory of Dark Matter and Space Astronomy, Purple Mountain Observatory, Chinese Academy of Sciences, Nanjing 210023, China*

[b]*School of Astronomy and Space Science, University of Science and Technology of China, Hefei 230026, China*

E-mail: mycui@pmo.ac.cn, xiajie@pmo.ac.cn, hejy@pmo.ac.cn

During the propagation of cosmic rays (CRs) in the solar system, they are blocked by the Sun and deflected by the magnetic field, resulting in a shadow on the celestial map. As CRs travel from the vicinity of the Sun to the Earth, they encounter deflection from the coronal magnetic field (CMF), the interplanetary magnetic field (IMF), and finally the geomagnetic field (GMF). The extent of deflection is determined by the magnetic field's intensity, direction, and energy of the CRs. Variations in the magnetic field cause corresponding changes in the position and size of the Sun's shadow . By observing the Sun's shadow of CRs, we can investigate the magnetic fields between the Sun and the Earth, complementing other measurements on these magnetic fields. Furthermore, it serves as a means to validate magnetic field models. The Large High Altitude Air Shower Observatory (LHAASO) is a new generation cosmic-ray and gamma-ray experiment in Daocheng, western China. With a vast Water Cherenkov Detector Array (WCDA) spanning 78,000 m^2, LHAASO can successfully observe the significant Sun's shadow within just a few days. Our study uses the WCDA to measure the Sun's shadow effect caused by CRs over multiple Carrington rotation periods. Subsequently, we compare these results with simulations based on different magnetic field models.

---

*Speaker

1. Introduction

The solar magnetic field is a crucial tool for studying solar physics. The calculation of the CMF is typically based on observations of the photosphere magnetogram and magnetic field models. Popular models for the CMF include the potential field source surface (PFSS) model [1] and the current sheet source surface (CSSS) model [2]. Previous observations have demonstrated that these models effectively describe the CMF during solar minimum. However, more precise observations are needed to further constrain the magnetic field models. The IMF is carried by the solar wind, which emanates from the Sun and fills the space between the Sun and the Earth. Previous measurements of the IMF have typically been made near the Earth, such as those obtained from the OMNI database [1]. Recently However, the Parker Solar Probe (PSP) now provides magnetic field measurements in proximity to the Sun [3]. The Parker model is widely employed to characterize the IMF [4]. Due to the CMF's role as a boundary condition, there is also uncertainty in calculating the IMF from the CMF. Furthermore, numerous modified models have been proposed for the IMF [5].

The origin of CRs remains a mystery even after a century since its discovery [6]. Prior to entering the solar system, CRs exhibit nearly isotropic distribution. Subsequently, they encounter obstruction from the Sun and undergo deflection by the magnetic field, resulting in the formation of a shadow on the CRs' sky map. Consequently, the Sun's shadow offers a valuable means to investigate the magnetic field in the region between the Sun and the Earth. Furthermore, given the cumulative effect of CRs' deflection in the magnetic field, it becomes possible to measure the overall structure and evolution of the magnetic field. Hence, this approach serves as a complementary method to local measurements such as those conducted by the OMNI and the PSP.

The characteristics of the Sun's shadow, such as displacement and extension, can be influenced by the Coronal Mass Ejections (CMEs) and the Interplanetary Magnetic Field (IMF). The relationship between the IMF and the displacement of the Sun's shadow has been studied by the ASγ collaboration [7–10]. The ARGO-YBJ collaboration has utilized the correlation between the Sun's shadow displacement and the IMF to indirectly measure the IMF and its sector structures [11]. Additionally, the deficit ratio is an important physical quantity in addition to the Sun's shadow displacement. The ASγ collaboration has found a relationship between the deficit ratio and solar activity, with their results supporting the CSSS model [12]. Both the ARGO-YBJ and ASγ collaborations have reported the rigidity-dependent features of the Sun's shadow [13, 14]. LHAASO, with its advantages of a wide energy range, high sensitivity, and large statistics, is able to observe the changes in the Sun's shadow with unprecedented sensitivity. In order to compare with the observations, a time dependent magnetic field model is proposed, and the simulations of the Sun's shadow are compared with the LHAASO observations.

2. Experiment and Data Analysis

The reconstruction of the direction and core position is crucial for analyzing CR air showers data. When a primary particle traverses through the atmosphere on top of the LHAASO array, it generates secondary particles that trigger the detectors. Subsequently, the time and integrated

---

charge of the triggered detectors are recorded as a "hit". Through the integration of the arrival time, charge, and positional information of the hits, we can determine the core position and direction of the primary particle.

2.1 Data Selection

To ensure the acquisition of high-quality data samples, we employed the following criteria:

(1) We selected publicly available data from the MK version dated March 5, 2021, to December 31, 2021.

(2) The ratio of "nbadq" to "ngoodq" must be less than 8×10^{-4}. Here, "ngoodq" represents the number of hits with good charge conversions, and "nbadq" represents the number of hits with bad charge conversions.

(3) The number of cells with an Npe value greater than 0.5 should exceed 100.

(4) We excluded data points with zenith angles outside the range of $5°$ to $45°$.

By employing the aforementioned criteria, the median energy of the dataset approximates 4 TeV.

2.2 Background Extinction

The purpose of background estimation in this study is to obtain the background for a specific region of the sky and determine the significance of the signal exceeding the background. The equi-zenith angle method is employed for this purpose. Within this band, we symmetrically select a specific number of circular regions on either side of the source region in the same zenith band, each being the same size as the source region. In this case, we choose six evenly distributed off-source windows with an angular distance of $5°$ from the source window. Both the source and off-source windows are divided into grid cells measuring $0.1° \times 0.1°$. The number of events falling into each cell is recorded.

We obtained one on-source map and six off-source maps. The maps were then smoothed using the Point Spread Function (PSF). Next, we applied the Li-Ma formula to calculate the significance, given by:

$$S = \sqrt{2} \left[N_{\text{on}} \ln \left(\frac{1+\alpha}{\alpha} \right) \left(\frac{N_{\text{on}}}{N_{\text{on}} + N_{\text{off}}} \right) \right) + N_{\text{off}} \ln(1+\alpha) \left(\frac{N_{\text{on}}}{N_{\text{on}} + N_{\text{off}}} \right) \right]^{1/2} \tag{1}$$

Here, N_{on}, N_{off}, and α represent the number of on-source events, the number of off-source events, and the scaling factor between the off-source and on-source, respectively.

2.3 Moon's Shadow

In Fig. 1, the left panel presents a significance sky map illustrating the Moon's shadow in April 2021. The most pronounced deficit is observed at the center, reaching a significance level of approximately 22σ. This indicates a noticeable eastward shift of the Moon's shadow center, amounting to approximately $0.58°$.

The analysis of the Sun's or Moon's shadow focuses on determining its position and extent. To achieve this, we project the events within a range of ±1 degree around the point of highest deficit significance onto the east-west or north-south direction, resulting in a one-dimensional distribution.
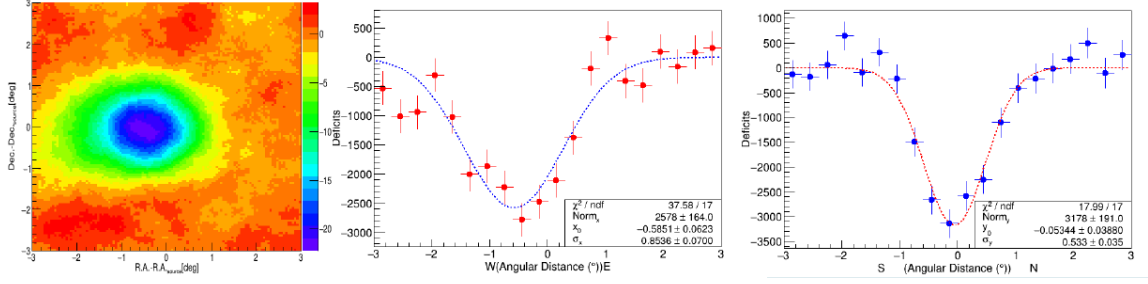
Figure 1: Left panel: the significance sky map of the Moon's shadow. Middle panel: the one-dimensional distribution in the east-west direction. Right panel: the one-dimensional distribution in the north-south direction.

These distributions can be fitted using a single (or double) Gaussian function, enabling us to ascertain the center of the shadow as well as the distribution's width. In Fig. 1, the middle and right panels display the one-dimensional distributions in the east-west and north-south directions, respectively.
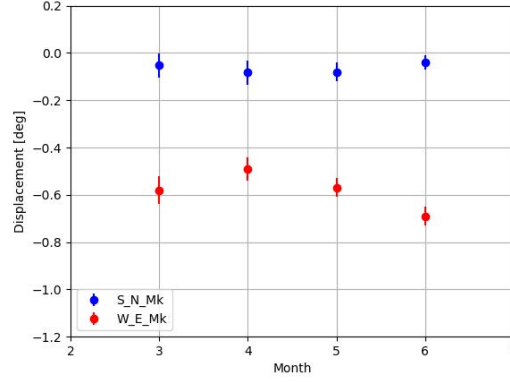

Figure 2: The one-dimensional projection of displacement of the Moon's shadow for different time intervals.

2.4 Observation of the Sun's Shadow

The significance sky map of the Sun's shadow from March 5th, 2021, to December 31st, 2021 is presented in the left panel of Fig. 3. The highest significance level reaches approximately -57 σ at the center. The middle and right panels in Fig. 3 display the one-dimensional distribution of the Sun's shadow in the east-west and north-south directions, respectively.

Thanks to its extensive statistical data, LHAASO has achieved an unprecedented ability to observe the Sun's shadow in just a few days.

3. Monte Carlo Simulation

3.1 Time-Dependent Magnetic Field

The observation of the Sun's shadow could be completed in just a few days, thereby requiring a corresponding time period for the magnetic field model in simulations. The magnetic field from
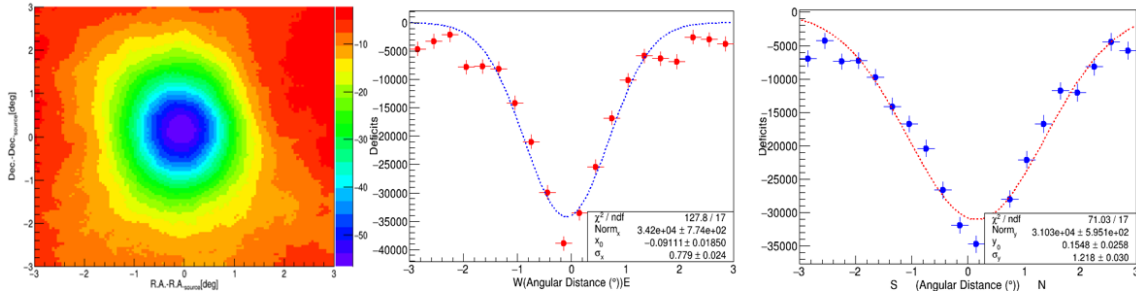
Figure 3: Left panel: the significance sky map of the Sun's shadow. Middle panel: the one-dimensional distribution in the east-west direction. Right panel: the one-dimensional distributions in the north-south direction

the Sun to the Earth can be categorized into three parts: the coronal magnetic field (CMF), the interplanetary magnetic field (IMF), and the geomagnetic field (GMF).

Traditionally, the CMF and IMF models used for simulations are assumed to remain constant during a solar rotation (SR). However, it is important to note that the CMF does undergo changes during a SR, and these changes can affect the IMF. Moreover, it takes time for the IMF to reach the Earth due to its transportation by the solar wind, which has a speed of about a few hundred kilometers per second. As a result, it typically takes several days for the solar wind to reach our earth.

On the other hand, cosmic ray (CR) particles are relativistic and can travel from the vicinity of the Sun to the Earth in just a few minutes. Therefore, when considering the magnetic field, it is crucial to account for its temporal variations.

In our study, we utilize the PFSS model and the CSSS model to analyze the Coronal Magnetic Field (CMF). The boundary condition, specifically the magnetic map of the photosphere, is obtained from observations made by the Helioseismic and Magnetic Imager (HMI) [1]. To ensure consistency, the time-dependent observations from the HMI are combined, resulting in a time bin of one day for the CMF model. Additionally, we set the source surface (R_{ss}) for the PFSS model and CSSS model as 2.5 $R_\odot$ and 10 $R_\odot$, respectively.

When studying the Interplanetary Magnetic Field (IMF), we employ the Parker model [2]:

$$
\begin{aligned}
B_r(r, \theta, \phi) &= B_r(R_{ss}, \theta, \phi_0)(\frac{R_{ss}}{r})^2 \\
B_\theta(r, \theta, \phi) &= 0 \\
B_\phi(r, \theta, \phi) &= -B_r(R_{ss}, \theta, \phi)(\frac{\Omega_{Sun}}{V_{sw}})(r - R_{ss})\sin\theta \\
\phi &= \phi_0 - \frac{R_{ss}\,\Omega_{Sun}}{V_{sw}}(\frac{r}{R_{ss}} - 1 - \ln(\frac{r}{R_{ss}}))
\end{aligned}
\tag{2}
$$

The equations of Parker model 2 are expressed in the Carrington coordinates and the V_{sw} represents speed of the solar wind. Since the CMF model is time dependent, the IMF is time dependent as a consequence, as is shown in equations 2. Currently, we consider the variation of solar wind speed with latitude only. The solar wind speed is measured using the interplanetary scintillation method [15]. For simplicity, we extend the results of year 2020 [15] to 2021 and study the CR 2243.

Furthermore, we use the International Geomagnetic Reference Field (IGRF) [16] to describe the GMF.
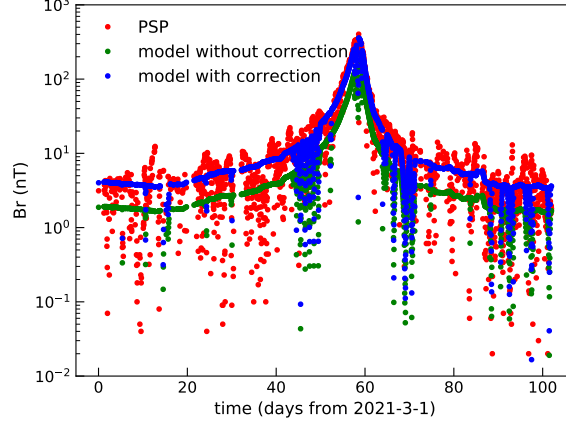

Figure 4: The correction of CSSS model prediction by PSP observation.

Finally, the CMF model tends to systematically underestimate the field strength, necessitating an overall correction of the model. The findings of the time-dependent Parker model are compared to the observations of the PSP[2] in Figure 4. Consequently, the IMF and CMF models are adjusted by scaling them with a constant derived from the data obtained from the PSP.

3.2 Simulation Method

We employ the "back tracing method" to simulate the Sun's shadow. Specifically, antiparticles are emitted in all directions within an angular range of $4° \times 4°$ around the Sun. To track the deflection of particles in the magnetic field, we utilize a fourth-order Runge-Kutta algorithm. If an antiparticle collides with the Sun, it is considered a "missing event." This indicates that a particle with an opposite charge cannot reach the Earth along the trajectory of the missing event. We collect these missing events to construct the simulated shadow of the Sun.

To align with the data analysis, we limit the zenith angle of particle launch from the Sun to a range of $5°$ to $45°$. To conserve computational resources, we exclude the simulation of the air shower and the subsequent reconstruction procedure. Instead, we utilize the point spread function (PSF) of the experiment.

The kinetic energy spectrum of incident particles is determined from both observation and simulation, with an average energy of approximately 4 TeV. Furthermore, the reconstructed energy follows an approximately logarithmic Gaussian distribution.

$$\log(E_{\text{k}}) \sim \text{N}(\mu = 0.6243, \sigma = 0.5548) \tag{3}$$

The formula for calculating the deficit ratio in simulations is as follows:

$$\text{deficit ratio} = \frac{N_{\text{hit with B}}}{N_{\text{all}}} \tag{4}$$

---

[2]https://cdaweb.gsfc.nasa.gov

In this equation, the numerator represents the number of events that hit the Sun in the presence of a magnetic field. The denominator, on the other hand, represents the total number of simulation events within a radius of $0.5°$ centered around the Sun.

3.3 Result

The following paragraph has been polished to meet academic writing standards, improving spelling, grammar, clarity, conciseness, and overall readability. Where necessary, sentences have been rewritten.

First, a Monte Carlo simulation is conducted to calculate the north-south displacement and deficit ratio of the Sun's shadow. The simulation results for these parameters are depicted in Fig. 5. It is evident that disparities exist between the results obtained from the CSSS and PFSS models. In the future, we intend to employ LHAASO observations to evaluate the magnetic field models.
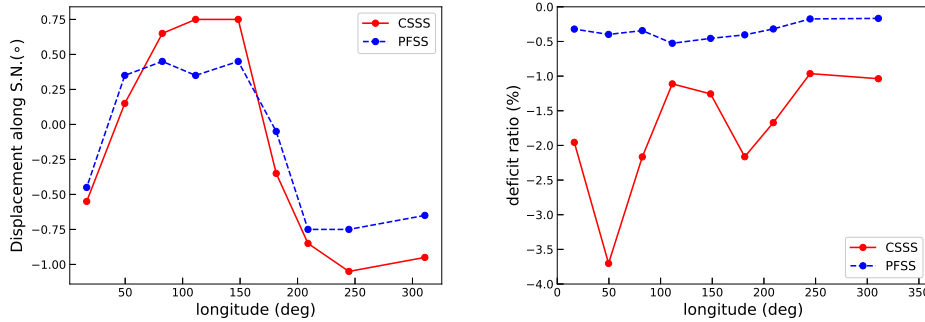

Figure 5: Simulation of the Sun shadow. The longitude is the Earth location in Carrington coordinate. Left panel: north-south displacement of the Sun shadow. Right panel: deficit ratio of the Sun shadow.

4. Summary

We conducted an analysis of the Moon shadow and Sun shadow based on observations from LHAASO. Additionally, we performed a Monte Carlo simulation to further investigate this phenomenon. We compared the influence of different models of the CMF on the simulated Sun shadow. In the future, we will present a systematic comparison between the observations and the simulation results.

5. Acknowledgement

References

[1] K. H. Schatten et al. 1969, Solar Physics, 6, 442

[2] X. Zhao, J. T. Hoeksema, 1995, Journal of Geophysical Research Space Physics, 100, 19

[3] N.E. Raouafi et al. 2023, Space Sci. Rev., 219:8

[4] E. N. Parker, 1958, Astrophysical Journal, 128, 677

[5] R. A. Burger et al. 2008, Astrophysical Journal, 674:511-519

[6] I. A. Grenier et al. 2007, Annu. Rev. Nucl. Part. Sci. 57:285–327

[7] M. Amenomori et al. 1993, Astrophysical Journal, 415, 147

[8] M. Amenomori et al. 1996, Astrophysical Journal, 464, 954

[9] M. Amenomori et al. 2000, Astrophysical Journal, 541, 1051

[10] M. Amenomori et al. 2009, Astrophysical Journal, 692, 61

[11] G. Aielli et al. 2011, Astrophysical Journal, 729

[12] M. Amenomori et. Al. 2013, Physical Review Letters, 111, 011101

[13] S. Z. Chen, Y. C. N. 2017, The 35th International Cosmic Ray Conference

[14] M. Amenomori et. Al. 2018, Physical Review Letters, 120, 031101

[15] C. Porowski, M. Bzowski, and M. Tokumaru, 2022, Astrophysical Journal Supplement Series, 259:2

[16] P. Alken et al. 2021, Earth Planets Space, 73, 49

Full Authors List: LHAASO Collaboration

Zhen Cao[1,2,3], F. Aharonian[4,5], Q. An[6,7], Axikegu[8], Y.X. Bai[1,3], Y.W. Bao[9], D. Bastieri[10], X.J. Bi[1,2,3], Y.J. Bi[1,3], J.T. Cai[10], Q. Cao[11], W.Y. Cao[7], Zhe Cao[6,7], J. Chang[12], J.F. Chang[1,3,6], A.M. Chen[13], E.S. Chen[1,2,3], Liang Chen[14], Lin Chen[8], Long Chen[8], M.J. Chen[1,3], M.L. Chen[1,3,6], Q.H. Chen[8], S.H. Chen[1,2,3], S.Z. Chen[1,3], T.L. Chen[15], Y. Chen[9], N. Cheng[1,3], Y.D. Cheng[1,3], M.Y. Cui[12], S.W. Cui[11], X.H. Cui[16], Y.D. Cui[17], B.Z. Dai[18], H.L. Dai[1,3,6], Z.G. Dai[7], Danzengluobu[15], D. della Volpe[19], X.Q. Dong[1,2,3], K.K. Duan[12], J.H. Fan[10], Y.Z. Fan[12], J. Fang[18], K. Fang[1,3], C.F. Feng[20], L. Feng[12], S.H. Feng[1,3], X.T. Feng[20], Y.L. Feng[15], S. Gabici[21], B. Gao[1,3], C.D. Gao[20], L.Q. Gao[1,2,3], Q. Gao[15], W. Gao[1,3], W.K. Gao[1,2,3], M.M. Ge[18], L.S. Geng[1,3], G. Giacinti[13], G.H. Gong[22], Q.B. Gou[1,3], M.H. Gu[1,3,6], F.L. Guo[14], X.L. Guo[8], Y.Q. Guo[1,3], Y.Y. Guo[12], Y.A. Han[23], H.H. He[1,2,3], H.N. He[12], J.Y. He[12], X.B. He[17], Y. He[8], M. Heller[19], Y.K. Hor[17], B.W. Hou[1,2,3], C. Hou[1,3], X. Hou[24], H.B. Hu[1,2,3], Q. Hu[7,12], S.C. Hu[1,2,3], D.H. Huang[8], T.Q. Huang[1,3], W.J. Huang[17], X.T. Huang[20], X.Y. Huang[12], Y. Huang[1,2,3], Z.C. Huang[8], X.L. Ji[1,3,6], H.Y. Jia[8], K. Jia[20], K. Jiang[6,7], X.W. Jiang[1,3], Z.J. Jiang[18], M. Jin[8], M.M. Kang[25], T. Ke[1,3], D. Kuleshov[26], K. Kurinov[26,27], B.B. Li[11], Cheng Li[6,7], Cong Li[1,3], D. Li[1,2,3], F. Li[1,3,6], H.B. Li[1,3], H.C. Li[1,3], H.Y. Li[7,12], J. Li[7,12], Jian Li[7], Jie Li[1,3,6], K. Li[1,3], W.L. Li[20], W.L. Li[13], X.R. Li[1,3], Xin Li[6,7], Y.Z. Li[1,2,3], Zhe Li[1,3], Zhuo Li[28], E.W. Liang[29], Y.F. Liang[29], S.J. Lin[17], B. Liu[7], C. Liu[1,3], D. Liu[20], H. Liu[8], H.D. Liu[23], J. Liu[1,3], J.L. Liu[1,3], J.Y. Liu[1,3], M.Y. Liu[15], R.Y. Liu[9], S.M. Liu[8], W. Liu[1,3], Y. Liu[10], Y.N. Liu[22], R. Lu[18], Q. Luo[17], H.K. Lv[1,3], B.Q. Ma[28], L.L. Ma[1,3], X.H. Ma[1,3], J.R. Mao[24], Z. Min[1,3], W. Mitthumsiri[30], H.J. Mu[23], Y.C. Nan[1,3], A. Neronov[21], Z.W. Ou[17], B.Y. Pang[8], P. Pattarakijwanich[30], Z.Y. Pei[10], M.Y. Qi[1,3], Y.Q. Qi[11], B.Q. Qiao[1,3], J.J. Qin[7], D. Ruffolo[30], A. Sáiz[30], D. Semikoz[21], C.Y. Shao[17], L. Shao[11], O. Shchegolev[26,27], X.D. Sheng[1,3], F.W. Shu[31], H.C. Song[28], Yu.V. Stenkin[26,27], V. Stepanov[26], Y. Su[12], Q.N. Sun[8], X.N. Sun[29], Z.B. Sun[32], P.H.T. Tam[17], Q.W. Tang[31], Z.B. Tang[6,7], W.W. Tian[2,16], C. Wang[32], C.B. Wang[8], G.W. Wang[7], H.G. Wang[10], H.H. Wang[17], J.C. Wang[24], K. Wang[9], L.P. Wang[20], L.Y. Wang[1,3], P.H. Wang[8], R. Wang[20], W. Wang[17], X.G. Wang[29], X.Y. Wang[9], Y. Wang[8], Y.D. Wang[1,3], Y.J. Wang[1,3], Z.H. Wang[25], Z.X. Wang[18], Zhen Wang[13], Zheng Wang[1,3,6], D.M. Wei[12], J.J. Wei[12], Y.J. Wei[1,2,3], T. Wen[18], C.Y. Wu[1,3], H.R. Wu[1,3], S. Wu[1,3], X.F. Wu[12], Y.S. Wu[7], S.Q. Xi[1,3], J. Xia[7,12], J.J. Xia[8], G.M. Xiang[2,14], D.X. Xiao[11], G. Xiao[1,3], G.G. Xin[1,3], Y.L. Xin[8], Y. Xing[14], Z. Xiong[1,2,3], D.L. Xu[13], R.F. Xu[1,2,3], R.X. Xu[28], W.L. Xu[25], L. Xue[20], D.H. Yan[18], J.Z. Yan[12], T. Yan[1,3], C.W. Yang[25], F. Yang[11], F.F. Yang[1,3,6], H.W. Yang[17], J.Y. Yang[17], L.L. Yang[17], M.J. Yang[1,3], R.Z. Yang[7], S.B. Yang[18], Y.H. Yao[25], Z.G. Yao[1,3], Y.M. Ye[22], L.Q. Yin[1,3], N. Yin[20], X.H. You[1,3], Z.Y. You[1,2,3], Y.H. Yu[7], Q. Yuan[12], H. Yue[1,2,3], H.D. Zeng[12], T.X. Zeng[1,3,6], W. Zeng[18], M. Zha[1,3], B.B. Zhang[9], F. Zhang[8], H.M. Zhang[9], H.Y. Zhang[1,3], J.L. Zhang[16], L.X. Zhang[10], Li Zhang[18], P.F. Zhang[18], P.P. Zhang[7,12], R. Zhang[7,12], S.B. Zhang[2,16], S.R. Zhang[11], S.S. Zhang[1,3], X. Zhang[9], X.P. Zhang[1,3], Y.F. Zhang[8], Yi Zhang[1,12], Yong Zhang[1,3], B. Zhao[8], J. Zhao[1,3], L. Zhao[6,7], L.Z. Zhao[11], S.P. Zhao[12,20], F. Zheng[32], B. Zhou[1,3], H. Zhou[13], J.N. Zhou[14], M. Zhou[31], P. Zhou[9], R. Zhou[25], X.X. Zhou[8], C.G. Zhu[20], F.R. Zhu[8], H. Zhu[16], K.J. Zhu[1,2,3,6], X. Zuo[1,3], (The LHAASO Collaboration)

[1] Key Laboratory of Particle Astrophyics & Experimental Physics Division & Computing Center, Institute of High Energy Physics, Chinese Academy of Sciences, 100049 Beijing, China
[2] University of Chinese Academy of Sciences, 100049 Beijing, China
[3] TIANFU Cosmic Ray Research Center, Chengdu, Sichuan, China

[4] Dublin Institute for Advanced Studies, 31 Fitzwilliam Place, 2 Dublin, Ireland

[5] Max-Planck-Institut for Nuclear Physics, P.O. Box 103980, 69029 Heidelberg, Germany

[6] State Key Laboratory of Particle Detection and Electronics, China

[7] University of Science and Technology of China, 230026 Hefei, Anhui, China

[8] School of Physical Science and Technology & School of Information Science and Technology, Southwest Jiaotong University, 610031 Chengdu, Sichuan, China

[9] School of Astronomy and Space Science, Nanjing University, 210023 Nanjing, Jiangsu, China

[10] Center for Astrophysics, Guangzhou University, 510006 Guangzhou, Guangdong, China

[11] Hebei Normal University, 050024 Shijiazhuang, Hebei, China

[12] Key Laboratory of Dark Matter and Space Astronomy & Key Laboratory of Radio Astronomy, Purple Mountain Observatory, Chinese Academy of Sciences, 210023 Nanjing, Jiangsu, China

[13] Tsung-Dao Lee Institute & School of Physics and Astronomy, Shanghai Jiao Tong University, 200240 Shanghai, China

[14] Key Laboratory for Research in Galaxies and Cosmology, Shanghai Astronomical Observatory, Chinese Academy of Sciences, 200030 Shanghai, China

[15] Key Laboratory of Cosmic Rays (Tibet University), Ministry of Education, 850000 Lhasa, Tibet, China

[16] National Astronomical Observatories, Chinese Academy of Sciences, 100101 Beijing, China

[17] School of Physics and Astronomy (Zhuhai) & School of Physics (Guangzhou) & Sino-French Institute of Nuclear Engineering and Technology (Zhuhai), Sun Yat-sen University, 519000 Zhuhai & 510275 Guangzhou, Guangdong, China

[18] School of Physics and Astronomy, Yunnan University, 650091 Kunming, Yunnan, China

[19] Département de Physique Nucléaire et Corpusculaire, Faculté de Sciences, Université de Genève, 24 Quai Ernest Ansermet, 1211 Geneva, Switzerland

[20] Institute of Frontier and Interdisciplinary Science, Shandong University, 266237 Qingdao, Shandong, China

[21] APC, Universit'e Paris Cit'e, CNRS/IN2P3, CEA/IRFU, Observatoire de Paris, 119 75205 Paris, France

[22] Department of Engineering Physics, Tsinghua University, 100084 Beijing, China

[23] School of Physics and Microelectronics, Zhengzhou University, 450001 Zhengzhou, Henan, China

[24] Yunnan Observatories, Chinese Academy of Sciences, 650216 Kunming, Yunnan, China

[25] College of Physics, Sichuan University, 610065 Chengdu, Sichuan, China

[26] Institute for Nuclear Research of Russian Academy of Sciences, 117312 Moscow, Russia

[27] Moscow Institute of Physics and Technology, 141700 Moscow, Russia

[28] School of Physics, Peking University, 100871 Beijing, China

[29] School of Physical Science and Technology, Guangxi University, 530004 Nanning, Guangxi, China

[30] Department of Physics, Faculty of Science, Mahidol University, 10400 Bangkok, Thailand

[31] Center for Relativistic Astrophysics and High Energy Physics, School of Physics and Materials Science & Institute of Space Science and Technology, Nanchang University, 330031 Nanchang, Jiangxi, China

[32] National Space Science Center, Chinese Academy of Sciences, 100190 Beijing, China